Materials & Design 212 (2021) 110207

Contents lists available at ScienceDirect

Materials & Design

journal homepage: www.elsevier.com/locate/matdes

A novel approach for microscale dry contact stiction and friction assessment: Experimentation and analysis

Bin Zhang [a], Reza Namakian [a], Xiaoman Zhang [a], W.J. Meng [a,*], Jennifer Hay [b], Kurt Johanns [b]

[a] Mechanical and Industrial Engineering Department, Louisiana State University, Baton Rouge, LA 70803, United States
[b] KLA Corp., Knoxville, TN 37922, United States

HIGHLIGHTS

- Compression molding and demolding test (CMDT), a novel method to assess micron scale dry contact stiction and friction, was presented.
- Micron scale stiction forces were measured and stiction stresses were examined in detail.
- Micron scale friction forces were measured, friction stress and friction coefficient were estimated by coupling experimental results with the cavity expansion model and FEM.
- Advantages and limitations of CMDT were discussed.

GRAPHICAL ABSTRACT

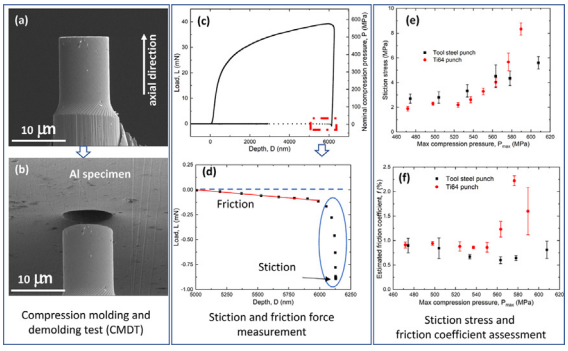

ARTICLE INFO

Article history:
Received 9 August 2021
Revised 14 October 2021
Accepted 27 October 2021
Available online 28 October 2021

Keywords:
Micro metal forming
Compression molding and demolding test
Measurement of stiction and friction forces
Microscale friction coefficient estimation

ABSTRACT

Accurate and quantitative evaluation of friction is of fundamental interest for materials science and manufacturing. Driven by the trend towards miniaturization, micro metal forming techniques with characteristic forming dimensions approaching a few microns have developed rapidly over the past two decades. In contrast, the assessment of microscale friction is lagging. Here, we present a novel test, compression molding and demolding test (CMDT), to assess stiction and friction at the microscale. CMDT was conducted via in-situ instrumented molding and demolding of an Al specimen with cylindrical tool steel and Ti alloy punches. High-rate data acquisition enabled direct measurements, for the first time, of microscale stiction and friction forces during disengagement between the punches and the molded Al under dry contact conditions. Stiction and friction stresses were then deduced and analyzed. The average friction coefficient was estimated by combining the cavity expansion model and finite element method analysis. Examinations suggest that punch geometry and surface finish, together with the accuracy of estimating the sidewall contact pressure, influence the obtained friction coefficient values. CMDT exhibits merits such as high operation simplicity and measurement accuracy and offers an alternative approach to providing new experimental evidence for a range of microscale friction problems.

© 2021 The Author(s). Published by Elsevier Ltd. This is an open access article under the CC BY-NC-ND license (http://creativecommons.org/licenses/by-nc-nd/4.0/).

1. Introduction

Friction is intricately intertwined with modern materials manufacturing processes, including metal forming operations [1] which possess advantages of high throughput and low cost. Metal forming techniques are characterized by large plastic strains and dis-

* Corresponding author.
E-mail address: wmeng1@lsu.edu (W.J. Meng).

https://doi.org/10.1016/j.matdes.2021.110207
0264-1275/© 2021 The Author(s). Published by Elsevier Ltd.
This is an open access article under the CC BY-NC-ND license (http://creativecommons.org/licenses/by-nc-nd/4.0/).

tinct relative motion between the forming tools and the deformed materials. Consequently, friction occurs at tool/material contact surfaces and significantly affects forming load, the surface quality of formed parts, and tool life [2]. Friction conditions are also important input parameters to models for simulating metal forming processes [3–5]. Friction is influenced by many factors, including tool materials, contact conditions, and surface finish, and is generally deemed difficult to quantify even in mature macroscale manufacturing processes [6].

The development of new friction tests has always been a focus of research [7–11]. Prevailing experimental methods for assessing friction in macroscale metal forming operations include the ring compression test (RCT) [7,9,12], the double cup extrusion test (DCET) [13], or combined forward and backward extrusion test (CFBET) [14], upsetting sliding test (UST) [15], and sliding compression test (SCT) [10]. RCT, DCET, and CFBET are indirect approaches, i.e., assessment of friction is accomplished by comparing experimentally measured dimensional changes of the loaded specimen with outputs of elastoplastic finite element analysis assuming different frictional characteristics. The measured geometric properties are the inner diameter changes before and after compression, the heights of extruded upper and lower cups, and the forward extruded rod length and backward extruded cup height in RCT, DCET, and CFBET, respectively. The limitations of these indirect friction tests are twofold: 1) it is difficult to precisely capture the specimen profile after testing, especially when severe inhomogeneous deformation occurs, which is common at large plastic strains [9]; 2) the assumed input parameters to generate the calibration curves may not fully reflect actual testing conditions [7]. UST and SCT are two commonly used direct methods in which friction coefficients are determined by measurement of the compression force and the tangential force [16].

Driven by the trend towards miniaturization, the last two decades have witnessed rapid development in micro metal forming techniques with characteristic forming dimensions ranging from millimeters to microns [17–20]. In contrast, the development of microscale friction testing is lagging significantly. Attempts to measure friction in micro metal forming operations have largely been limited to miniaturizing macroscale compression- or extrusion- based testing protocols, e.g., by conducting DCET tests with specimen diameter decreasing from a few mm down to $\sim$ 0.5 mm [21]. The disadvantages of macroscale friction assessment persist and are exacerbated when attempting to miniaturize such tests. On one hand, such miniaturized friction tests become increasingly difficult to execute and less accurate as the characteristic specimen dimension decreases to the sub-mm scale or smaller. For example, UST is performed on wires and its usability is limited. On the other hand, the external size of specimens may influence the friction conditions in micro forming, making microscale friction evaluation more complicated. For instance, Tiesler and Engel reported that friction increased significantly with decreasing specimen size in micro-compression, micro-extrusion, and micro-drawing tests with oil lubricants, which they rationalized with an open and closed lubricant pockets model [22,23]. Furthermore, experimental data on friction under dry contact conditions are limited [24,25]. The paucity of appropriate microscale friction tests and experimental data impedes an in-depth understanding of the mechanical response and deformation behavior in micro metal forming operations, thus limiting further development of micro metal forming techniques [26]. Therefore, devising new friction tests for micro metal forming processes is of significant scientific and engineering interest.

In this paper, we present in detail a novel approach to evaluating dry contract friction at the micron scale, namely, the compression molding and demolding test (CMDT). CMDT is a two-stage process, as displayed schematically in Fig. 1. In the compression molding process, a microscale non-deforming cylindrical punch is compressed into a metallic specimen (Fig. 1(a)), reaching a penetration depth D at a compression load L, and in the process creating punch/specimen sidewall contact (Fig. 1(b)). The subsequent demolding process involves a sliding contact between the punch and the specimen sidewall surfaces. Measurement of the pullout force, F, thus allows for direct measurement of the friction force, since F_f =(-1) F during punch pullout (Fig. 1(c)). Friction stress, τ_f, can then be computed by knowing the punch sliding distance, D_c. A friction coefficient f can then be determined if the punch/specimen sidewall contact pressure σ_n is known (Fig. 1(d)), assuming that the Coulomb's law of friction holds [24]. In what follows, we will report the results and analysis of CMDT performed on an Al sample using microscale cylindrical punches made of tool steel and a Ti alloy.

2. Experimental procedures

Instrumented CMDTs were carried out in-situ an FEI Quanta3D FEG Dual-Beam scanning electron microscope/Ga^+ focused ion beam (SEM/FIB) instrument using a NanoMechanics NanoFlip nano/micro mechanical testing system. Cylindrical micro punches were fabricated out of a commercial tool steel rod with a bulk hardness of HRC 60 and a commercial Ti-6Al-4 V alloy (Ti64) using established Ga^+ FIB lathe milling procedures [27]. Fig. 2(a) shows one finished tool steel punch with a radius R of 4.635 μm and a length of $\sim$ 12 μm. As evident in Fig. 2(a), the finished punch possesses a flat top surface and a sharp transition from the flat top to a smooth and straight cylindrical sidewall. Fig. 2(b) shows one finished Ti64 punch with a radius R of 4.93 μm and a length of $\sim$ 14 μm, with similar morphological features. Finished punches were mounted onto the NanoFlip actuator and used to mold a ⟨1 1 0⟩ oriented single crystal Al specimen.

The actual molding and demolding process was controlled by the NanoFlip instrument in a force-controlled mode. The entire experiment was divided into an approach segment, a molding segment, and a demolding segment. In the approach segment, the punch was placed in front of the Al specimen at a distance of $\sim$ 2 μm, then driven by the NanoFlip actuator to approach the specimen surface, with the displacement of and load on the punch measured continuously at a rate of 100 Hz. The NanoFlip instrument detected contact between the punch and the specimen surface through contact stiffness changes. Once contact was detected, the instrument transitioned into the molding segment. In the molding segment, the punch load was increased at a constant rate of 0.5 mN/s until a preset maximum load was reached while punch displacement and load were measured continuously at a rate of 200 Hz. Once the maximum load was reached, the instrument transitioned into the demolding segment without holding. In the demolding segment, punch load was decreased at a constant rate of 0.5 mN/s until the punch was 2000 nm away from the specimen surface, completely disengaged. Two videos in the Supplemental Materials section, entitled "approach and molding segments" and "demolding segment", give a visual illustration of these two processes, respectively.

A typical configuration of the tool steel punch after demolding, together with the hole created within the Al specimen, is shown in Fig. 2(c). No deformation of the punch was observed after multiple molding runs. The typical morphology of molded micro holes in the Al specimen is illustrated in Fig. 2(d). The molded hole is seen to possess a flat bottom, apparently straight sidewall, and a sharp sidewall to bottom transition. The morphology of the bottom surface is identical to that of the unmolded specimen top surface, consistent with the expectation that the specimen top surface region in contact with the punch travels down with the punch without

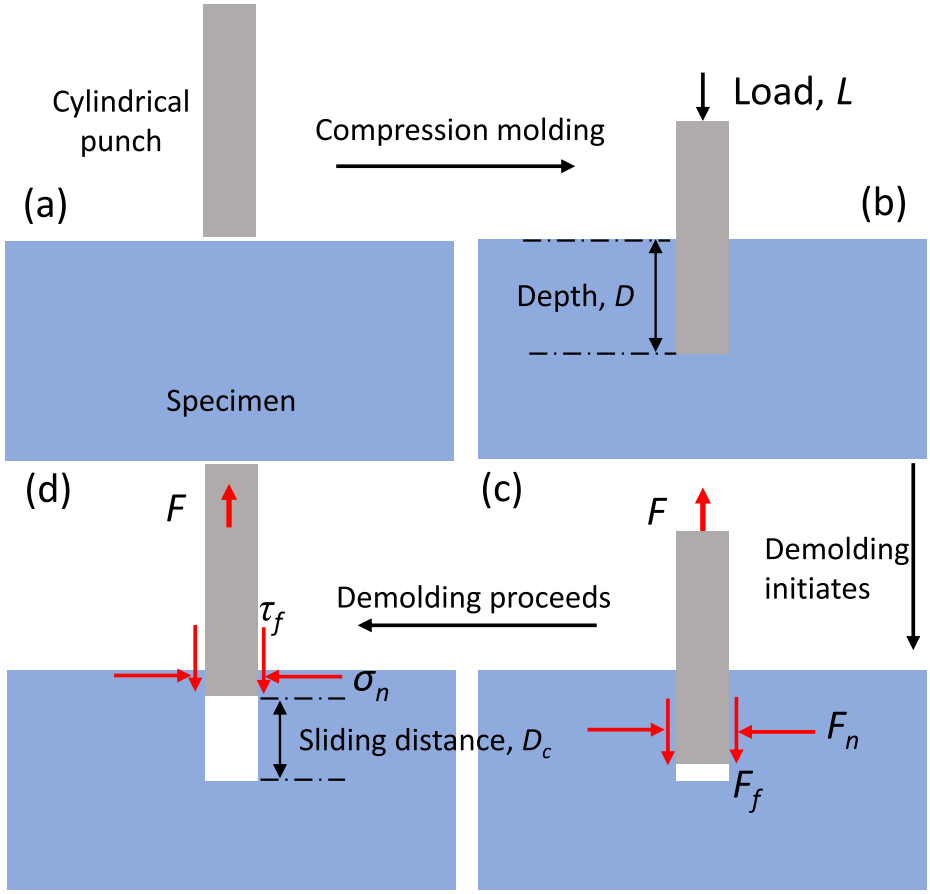

Fig. 1. A schematic illustration of the compression molding and demolding test (CMDT).

relative motion in a "dead plug" fashion [19]. Striations along the axial direction of the hole are apparent on the sidewall surface, indicative of relative motion between the punch and the molded hole along the axial direction during the molding/demolding process. Similar observations were made when the Ti64 punch was used.

The actual process of disengagement between the punch and the Al specimen was observed to occur so rapidly that a data acquisition rate of 200 Hz was incapable of capturing a sufficient amount of punch displacement and load data. Therefore, the rate of punch displacement and load measurement was set at 200 Hz in the initial portion of the demolding segment and increased to 10 kHz in the final portion of the demolding segment using the DataBurst data-acquisition capability of the NanoFlip instrument.

The experimentally observed rapid punch disengagement process means that the NanoFlip actuator, on which the punch is mounted, experiences significant velocity and acceleration during punch pull-out. Therefore, significant dynamic forces may be present during disengagement. A short exposition of how the NanoFlip instrument obtains the actual reaction force due to punch contact with the specimen is thus in order. The NanoFlip actuation system is designed to approximate a simple harmonic oscillator, allowing only one dimension of motion, x, relative to a neutral position $x = 0$. At any time, the forces acting on the actuator satisfy

$$F_e + mg = Kx + C\dot{x} + m\ddot{x} + R_c, \tag{1}$$

where F_e is the system-induced electromagnetic actuation force, mg is the gravitational force, K is the effective stiffness of the springs supporting the actuator column, C is the effective damping of the actuator, m is the effective actuator mass, R_c is the reaction force due to contact of the punch with the specimen, and x, $\dot{x}$, and $\ddot{x}$ are respectively the position, velocity, and acceleration of the mass. In practice, these forces are measured by referencing to their values at initial punch/specimen contact, at which point the forces are

$$F_{ec} + mg = Kx_c, \tag{2}$$

the damping, inertial, and reaction forces being negligibly small at initial punch/specimen contact. To know the forces acting on the punch relative to the contact point, Eq. (2) is subtracted from Eq. (1) and rearranged to solve for the quantity of interest, namely R_c. This yields

$$R_c = (F_e - F_{ec}) - K(x - x_c) + C\dot{x} + m\ddot{x}. \tag{3}$$

This reaction force delivered by punch/specimen contact, R_c, is reported as the "punch load", L. In most experiments, the damping and inertial terms in Eq. (3) are negligible because the actuator velocity and acceleration are small. But in the current experiments, the punch motion as it is withdrawn from the molded specimen is such that all terms in Eq. (3) are relevant.

The load is zero when the indenter loses contact with the specimen, $R_c = L = 0$. That the value calculated by the right-hand side of Eq. (3) under non-contact conditions is in fact zero, or very nearly so, is a verification of the validity of the simple harmonic oscillator model for the actuator system, the model parameter values (K, C, and m), and the determination of the initial punch/specimen contact (F_{ec}, x_c). Conversely, any deviation from zero of the right-hand side of Eq. (3) under punch/specimen non-contact situations reveals limitations in modeling the dynamics of the actuator system. In the present set of experiments, the values of the simple-

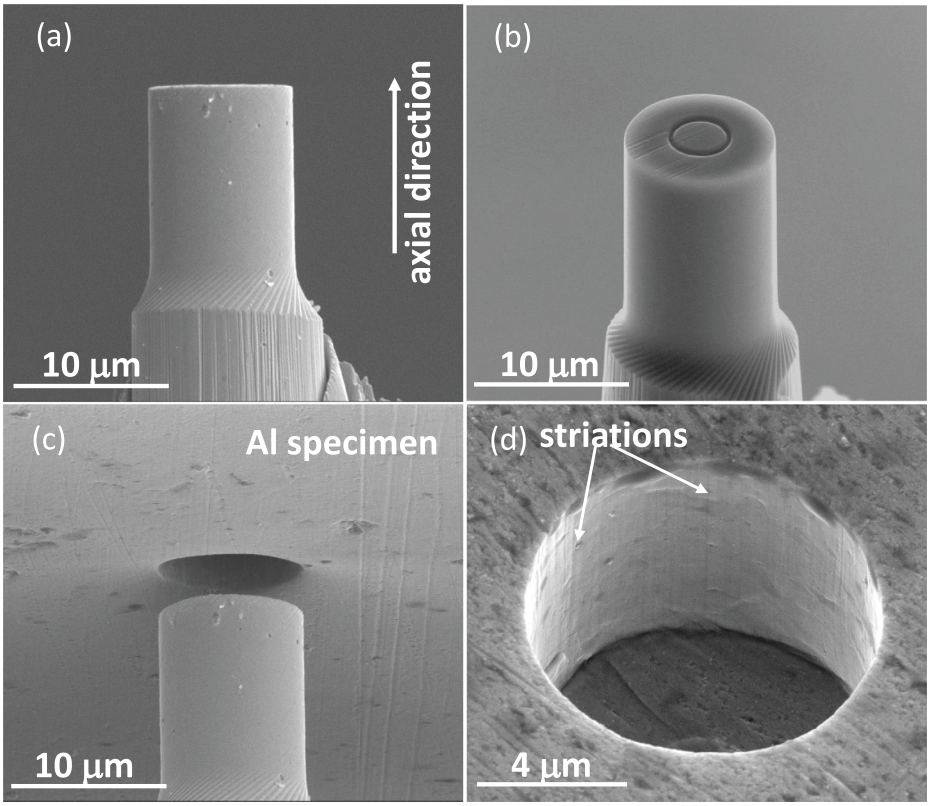

Fig. 2. Microscale instrumented molding/demolding of a single crystal Al specimen by cylindrical punches: (a) a sideview of the FIB-milled cylindrical tool steel punch with a diameter of 9.27 μm and a length of ~ 12 μm; (b) a 52° tilted view of the FIB-milled cylindrical Ti64 punch with a diameter of 9.86 μm and a length of ~ 14 μm; (c) a 15° tilted view of the same tool steel punch and the formed hole in the Al specimen; (d) a 35° tilted view of a typical micro hole in the Al specimen molded by the tool steel punch.

harmonic oscillator model parameters are determined through prior calibration by the instrument manufacturer.

3. Results

3.1. Compression molding/demolding processes

Results of a typical CMDT run on the single crystal Al specimen with the cylindrical tool steel punch are illustrated in Fig. 3. Fig. 3 (a) shows the measured punch load, L, vs. time, t, in the upper panel, and the derivative dL/dt vs. t in the lower panel. Positive and negative L values denote a compressive and a tensile load on the punch, respectively. Arrows labeled 1 through 4 denote in sequence instants when the loading segment started, when the unloading segment started, when the 10 kHz high-rate data-acquisition began, and when separation between the punch and the molded Al specimen occurred (a large peak in dL/dt). The approach, molding, and demolding segments are represented by the time sequence before arrow 1, between arrows 1 and 2, and after arrows 2, respectively. During the approach segment, $-25\ s < t < 0\ s$, L values hovered around zero, with $|L| < 1\ \mu N$. In the molding segment, the maximum compression load, L_{max}, was set to be + 39 mN, as marked by arrow 2. In the demolding segment, the transition from data taking at a rate of 200 Hz to 10 kHz, marked by arrow 3, led to an appreciable change in the noise floor of dL/dt, due to the much shorter data-taking time step.

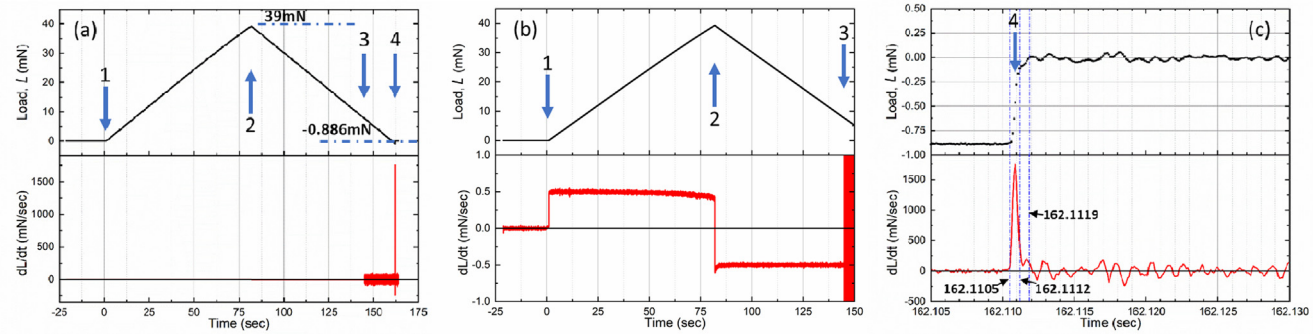

Fig. 3. A typical microscale instrumented Al molding/demolding experiment with the tool steel punch: (a) load L vs. time t (upper panel) and dL/dt vs. t (lower panel); (b) expanded views of L vs. t in the range of $-25\ s < t < 150\ s$, with L and dL/dt displayed respectively in upper and lower panels; (c) expanded views of L vs. t and in the range of $162.1050\ s < t < 162.1300\ s$, with L and dL/dt displayed respectively in upper and lower panels.

Arrow 4 marks the instant when dL/dt exhibits a significant peak. The actual demolding event, as explained in more detail below, occurred close to the instant marked by arrow 4. Unloading in the demolding segment brought L from + 39 mN to ∼ − 0.886 mN before punch/specimen separation occurred, indicating that a tensile pull was necessary for the punch to disengage from the molded specimen.

Fig. 3(b) plots expanded views of the same L vs. t data shown in Fig. 3(a), before the actual punch/specimen disengagement occurred. The dL/dt plot shown in Fig. 3(b) displays clearly the loading and unloading rates of 0.5 mN/s in the molding and demolding segments, respectively. Fig. 3(c) plots expanded views of the same L vs. t shown in Fig. 3(a), close to the actual event of punch/specimen disengagement. Prior to the peak in dL/dt, the punch load stayed relatively constant at ∼ − 0.886 mN, i.e., the punch was subjected to a tensile pull. Within a duration of 0.7 ms, from t = 162.1105 s to t = 162.1112 s, this tensile pull, |L|, decreased from 0.877 mN to 0.114 mN. In the next 0.7 ms, from t = 162.1112 s to t = 162.1119 s, |L| decreased at a slower rate from 0.114 mN to 0.004 mN. After that, L values and the corresponding dL/dt values hovered around zero, indicating a complete punch/specimen disengagement.

Fig. 4(a) displays the corresponding measurement of punch displacement, D, vs. t in the upper panel, while the lower panel shows the derivative dD/dt vs. t, with D > 0 and D < 0 implying respectively that the punch is below and above the original specimen's surface. The approaching displacement rate was 100 nm/s (before arrow 1). At the point of punch/specimen contact, D was set to be zero (arrow 1). Once the molding segment commenced, D increased slowly in the beginning when the material's response is largely elastic. As L continued to increase, D increased faster with time as extensive plastic deformation occurred. At the end of the molding segment, L = +39 mN, the largest D value was 6267 nm (arrow 2). The inset displays in more detail the demolding segment before actual punch/specimen disengagement occurred. Unloading punch compression from + 39 mN to ∼ 0 mN brought a corresponding change in D value from 6267 nm to 6140 nm: a depth decrease of 127 nm. As the demolding segment continued, L changed further from ∼ 0 mN to ∼ − 0.886 mN with a corresponding change in D value from 6140 nm to 6128 nm, a further decrease in depth of 12 nm. The entire 139 nm displacement occurred without relative punch/specimen motion. Thus D = 6128 nm should represent the molding depth D_{max}.

Fig. 4(b) plots expanded views of the same D vs. t data shown in Fig. 4(a), before the actual punch/specimen disengagement occurred. The average dD/dt value in the approach segment, before arrow 1, is consistent with the set punch displacement rate of 100 nm/s. At arrow 3, the increase in the noise floor of dD/dt is again coincident with the data acquisition rate transition from 200 Hz to 10 kHz. Fig. 4(c) plots expanded views of the same D vs. t data shown in Fig. 4(a), close to the actual event of punch/specimen disengagement. Within a duration of 0.7 ms, from t = 162.1105 s to t = 162.1112 s, where the rapid decrease in |L| was observed, D changed from 6128 nm to 5988 nm, and the punch traveled a distance of 140 nm at an average speed of 200 nm/ms. In the next 0.7 ms, from t = 162.1112 s to t = 162.1119 s, where |L| decreased at a slower rate from 0.114 mN to 0.004 mN, D changed from 5988 nm to 5008 nm, and the punch traveled a distance of 980 nm at an average speed of 1400 nm/ms. From t = 162.1119 s to t = 162.1300 s, D exhibited a damped oscillatory behavior with significant amplitudes: first decreasing from 5008 nm to one peak displacement of 376 nm, then increasing again to another peak displacement of 2912 nm, followed by two additional oscillations with further diminished amplitudes with peak displacements of 1887 nm and 2141 nm. The maximum actuator speeds associated with these oscillations are ∼ 2400 nm/ms, ∼1100 nm/ms, ∼430 nm/ms, ∼120 nm/ms, respectively.

3.2. Stiction and friction measurements

Fig. 5(a) replots the tool steel punch dataset shown in detail in Figs. 3 and 4, in terms of the measured punch load and the calculated nominal compression pressure, $p = L/\left(\pi R^2\right)$, as a function of the molding depth D during the entire CMDT run. The molding portion of the L vs. D curve is qualitatively in agreement with previous instrumented microscale molding experiments, i.e., the L–D curve exhibits a rapid initial rise in L with increasing D when the specimen molding response is largely elastic, followed by a bend-over after which L increases more slowly with increasing D when large scale plastic deformation occurs within the molded specimen [17,28]. Fig. 5(b) shows an expanded view of the portion of the tool steel punch L-D curve where actual punch/specimen disengagement occurred, shown in Fig. 5(a) within the dashed red square.

Recall that stiction, or static friction, refers to the phenomenon that a force is required to initiate relative motion between two contacting bodies at rest [29], we state that the maximum tensile load, |L|, experienced by the punch before relative punch/specimen motion was initiated, yields a measure of the stiction force. In other words, the measured tensile load at the maximum molding depth is the stiction force. As indicated by the black arrow in Fig. 5(b), the stiction force, F_s, is 0.886 mN at D_{max} = 6128 nm. Once the stiction is overcome, the steel punch travels a short distance,

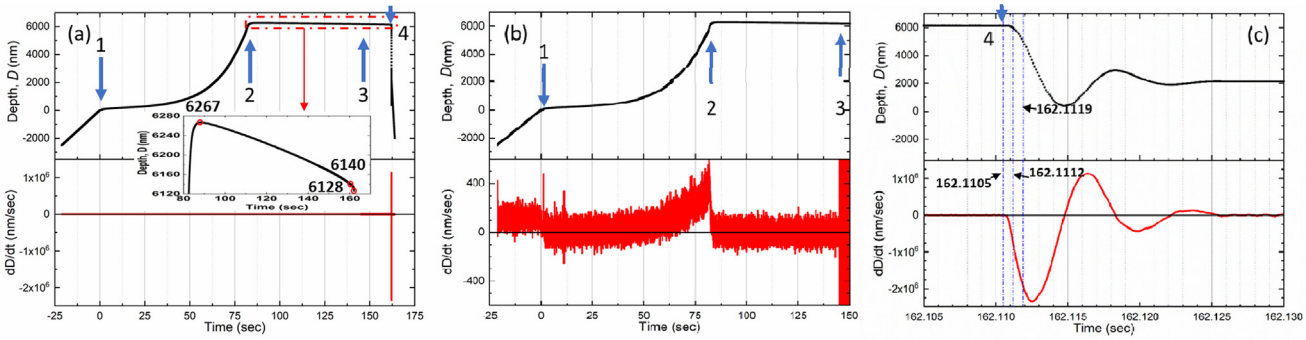

Fig. 4. A typical microscale instrumented Al molding/demolding experiment with the tool steel punch: (a) punch molding depth D vs. t (upper panel) and dD/dt vs. t (lower panel). The inset shows an expanded view of the data portion highlighted in the red dashed rectangle; (b) expanded views of D vs. t in the range of −25 s < t < 150 s, with D and dD/dt displayed respectively in upper and lower panels; (c) expanded views of D vs. t in the range of 162.1050 s < t < 162.1300 s, with D and dD/dt displayed respectively in upper and lower panels. (For interpretation of the references to colour in this figure legend, the reader is referred to the web version of this article.)

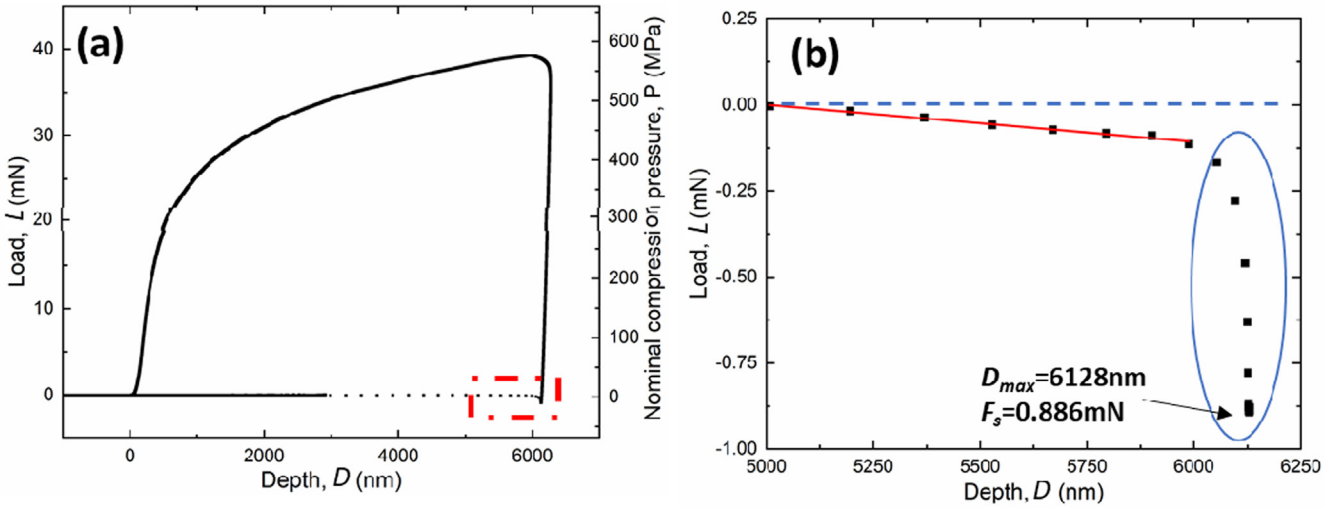

Fig. 5. Replotting the microscale instrumented Al molding/demolding dataset obtained using the tool steel punch: (a) *L* vs. *D* during the entire molding and demolding cycle; (b) an expanded view of the demolding data portion highlighted in the red dashed rectangle in (a). The dashed blue line in (b) gives a visual guide to the zero-load level. (For interpretation of the references to colour in this figure legend, the reader is referred to the web version of this article.)

ΔD_s, of 140 nm (from 6128 nm to 5988 nm), accompanied by a significant drop in $|L|$ value from 0.877 mN to 0.114 mN. The corresponding data segment is within the blue circle in Fig. 5(b).

Recall that friction, or kinetic friction, refers to the phenomenon that a force is required to keep two contacting bodies in relative motion [29], we state that the decreasing $|L|$ values while the punch was pulled out of the specimen after stiction was overcome yield a measure of the friction force, F_f, associated with the punch/specimen sliding contact, i.e., $|L| = F_f$. Therefore, the measured punch response curve within the load range of 0.114 mN > $|L|$ > 0.004 mN and the displacement range of 5988 nm > *D* > 5008 nm, is dominated by friction between sidewall surfaces of the punch and the molded hole. The sliding distance, D_c, is 980 nm. The data segment conforms well to a linear fit, as indicated in Fig. 5(b) by the red line fitting the data points.

Fig. 6 presents a CMDT dataset generated using the Ti64 punch with L_{max} set at 41 mN. It is clear that the dataset exhibits features completely analogous to those described in Fig. 5. Thus, for the Ti64 punch experiments, only the results are presented without showing the detailed data analysis steps as shown for the tool steel punch experiments in Figs. 3, 4, and 5.

3.3. Sliding distance assessments

Fig. 7(a) shows a schematic illustration of the punch demolding process based on the detailed exposition of the data shown in Figs. 3, 4, 5, and 6: 1) stiction is overcome in a short distance, ΔD_s, with a concomitant tensile load drop; 2) $|L|$ then decreases to zero over a sliding distance or contact distance, D_c, within which sliding friction between the punch sidewall surfaces and the molded specimen dominates; 3) the intercept value on the *D* axis from the linear fit, *Int*, where $|L|$ becomes zero denotes the point of complete punch/specimen disengagement.

Two series of CMDT experiments were carried out: a total of 21 independent CMDT runs using the tool steel punch and a total of 25 independent CMDT runs using the Ti64 punch on the same single crystal Al specimen with varying L_{max} values. All raw datasets, i.e., *L* vs. *t* and *D* vs. *t*, are qualitatively similar to the data shown in

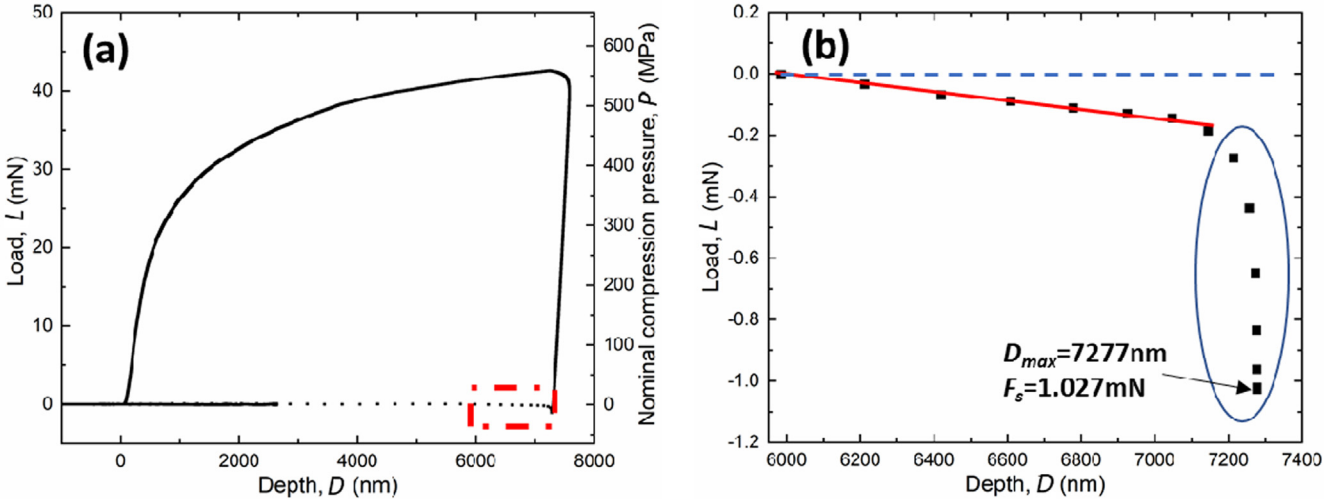

Fig. 6. An instrumented Al molding/demolding dataset obtained using the Ti64 punch: (a) *L* vs. *D* during the entire molding and demolding cycle; (b) an expanded view of the demolding data portions highlighted in the red dashed rectangle in (a). The dashed blue line in (b) gives a visual guide to the zero-load level. (For interpretation of the references to colour in this figure legend, the reader is referred to the web version of this article.)

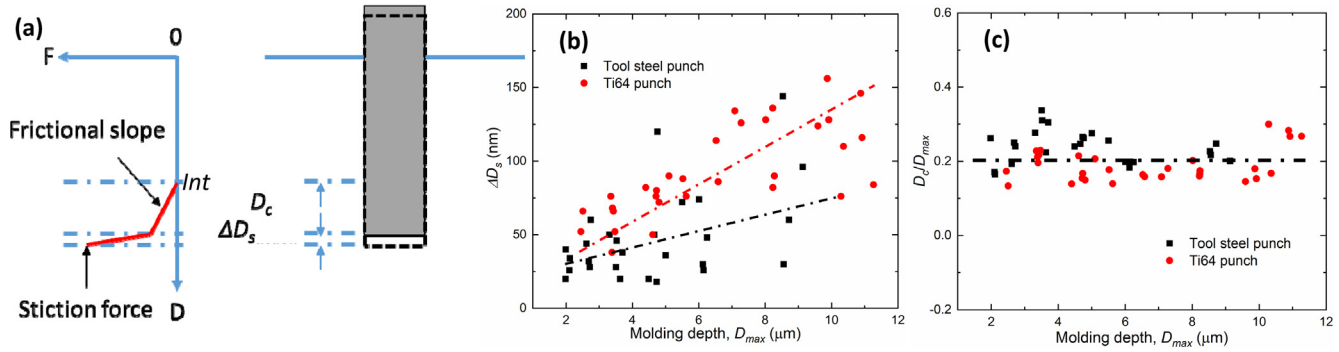

Fig. 7. The punch demolding process: (a) a schematic illustration of the entire demolding process: ΔD_s, D_c, and *Int* denote the punch travel distance over which stiction was overcome, the distance over which the punch/specimen sidewalls were in sliding contact, and the depth at which the punch became free (load became zero), respectively; (b) ΔD_s vs. D_{max}; (c) D_c/D_{max} vs. D_{max}. The dash lines in (b) and (c) are guides to the eye.

Figs. 3 and 4, and processed in the same way. Fig. 7(b) plots measured ΔD_s values vs. D_{max}, for both the tool steel and Ti64 punch cases. It is evident that ΔD_s shows a slight increase as D_{max} increases. Despite the data scatter, ΔD_s for the Ti64 punch appears to be higher than that for the tool steel punch at the same molding depth. For all cases, ΔD_s is < 160 nm, indicating $\Delta D_s \ll D_{max}$ holds true for all data points displayed in Fig. 7(b). Fig. 7(c) plots the ratio of D_c/D_{max} vs. D_{max}. This ratio, viewed from the results of a total of 46 independent molding/demolding measurements, is seen to be approximately a constant, ~0.2, over a large range of D_{max} values.

During punch/specimen disengagement, the cylindrical punch would be expected to maintain sidewall contact with the molded hole through the entire molding depth if the punch is shaped like a geometrically perfect cylinder. This is contrary to the data shown in Fig. 7(c) that the contact depth is significantly less than the molding depth. As shown in Figs. 3 and 4, the fact that the punch reentered the hole to a depth of 2912 nm during the free oscillation after disengagement without encountering a reaction force from the specimen is also consistent with contact loss at D < 5000 nm. These observations suggest that the actual tool steel and Ti64 punches possess slight tapers instead of having perfect cylindrical shapes, even though such tapers are hard to perceive from images shown in Fig. 2. Furthermore, D_c/D_{max} values from the tool steel punch case largely overlap those from the Ti64 punch case, suggesting that the taper existing in the tool steel and Ti64 punches is similar, which can be attributed to the same FIB milling procedure for punch fabrication.

4. Discussion

4.1. Stiction stress evaluation

According to the schematic of the demolding process shown in Fig. 7(a), the measured stiction force F_s can be converted to a nominal stiction stress,

$$\sigma_s = \frac{F_s}{\pi R^2 + 2\pi R D_{max}}. \quad (4)$$

Here we assume that full top/bottom and sidewall contact between the punch and the molded material is in effect before stiction is overcome. Fig. 8 plots this nominal stiction stress as a function of the corresponding nominal maximum compression pressure, given by

$$P_{max} = \frac{L_{max}}{\pi R^2}. \quad (5)$$

The nominal stiction stress increases with increasing P_{max} in both cases and possesses close values at P_{max} < 540 MPa. As P_{max} increases further to over ~ 570 MPa, the nominal stiction stress for the Ti64 punch increases above that for the tool steel punch, exceeding 8 MPa while all stiction stress values for the tool steel punch stayed below 6.2 MPa.

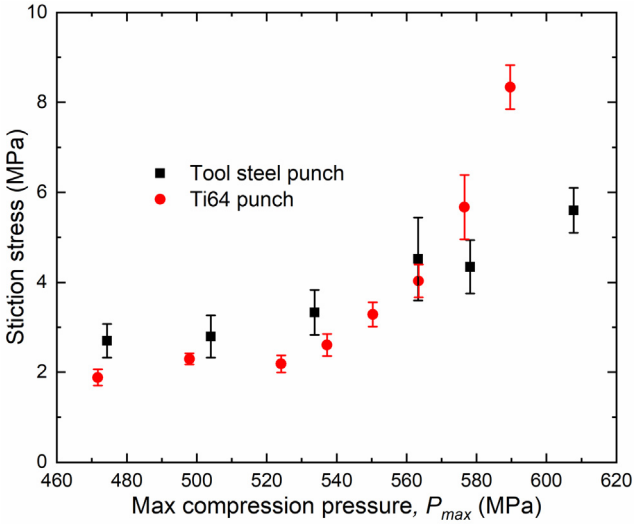

Fig. 8. The nominal stiction stress vs. the maximum compression pressure on the punch.

The stiction phenomenon has been intensely studied in the context of microelectromechanical systems (MEMS) devices fabricated by surface micromachining [30]. Failure of surface micromachined devices results when suspended microscale polycrystalline silicon (polySi) structures stick to and unable to separate from the silicon substrate due to adhesion [31]. For polySi, apparent work of adhesion, W_{ad}, has been measured using a cantilever beam array (CBA) technique to range from 10 μJ/m^2 to 20 mJ/m^2, depending on surface chemistry and topography [32]. A W_{ad} value of 56 mJ/m^2 was also measured by the CBA technique for polySi microstructures with oxide coated surfaces [33]. In addition to MEMS devices, another instance where quantitative measurements related to stiction are performed is the evaluation of single asperity contact using scanning force microscopy. For example, an atomic force microscope (AFM) can be used to monitor the situation when a sharp tip with radius ranging from 10 to 100 nm is brought to contact with a surface. The critical force needed to pull the tip off the surface yields a measure of the work of adhesion [34]. Jiang and Turner used AFM measurements to yield a W_{ad} value of ~ 50 mJ/m^2 between an ultra-nanocrystalline diamond (UNCD) tip and a PMMA (polymethylmethacrylate) surface. An effective adhesive stress, σ_D, was also obtained by extracting an adhesion range

parameter h_{ad}, with $\sigma_D = W_{ad}/h_{ad}$. For the UNCD/PMMA contact, the extracted σ_D value is ~ 20 MPa [35]. While both the CBA and the AFM methods deal with separation of two surfaces along approximately the normal direction, it is noted that overcoming stiction in the present punch/specimen contact situation involves normal separation between the punch top surface and the molded hole bottom surface as well as shear motion between the sidewall surfaces of the punch and the molded hole. Further, the actual contact area between the punch and the molded hole will not be the nominal contact area, $\left(\pi R^2 + 2\pi RD_{max}\right)$, as the punch does not possess a geometrically smooth surface. Rather, we expect that the actual contact area to increase as P_{max} increases, as is well known for rough surfaces in contact [3,24]. The increase in the nominal stiction stress shown in Fig. 8 as P_{max} increases thus seems reasonable. The range of nominal stiction stress values, 2 ~ 8 MPa, also appears reasonable in view of the CBA and AFM measurement values cited above. In addition, the fact that the stiction stress is higher for the Ti64 punch at P_{max} > 570 MPa is consistent with the expectation of Ti having a stronger chemical affinity with Al as compared to Fe, as judged by ranking the maximum heat of formation in Ti- and Fe-aluminides [36].

4.2. Evaluation of friction stress and friction coefficient

During the demolding process after stiction has been overcome, sliding friction between the punch sidewall and the molded material dominates. As shown in Fig. 1, the pull-out force F sensed by the instrument provides a direct measure of the friction force,

$$(-1)F = F_f \tag{6}$$

The Coulomb's law of friction states that

$$F_f = f\ F_n, \tag{7}$$

where f is the friction coefficient. Dividing both sides of Eq. (7) by the contact area $2\pi RD_c$, we have

$$\tau_f = f\sigma_n, \tag{8}$$

where σ_n is the normal stress applied on the punch sidewall surface by the molded specimen or the contact pressure, and τ_f is the friction stress (see Fig. 1). As the contact area is $2\pi RD_c$, the frictional force during punch pull-out is

$$(-1)F = \tau_f 2\pi RD_c \tag{9}$$

From Eq. (9), the friction stress is obtained,

$$\tau f = \frac{-1}{2\pi R}\frac{dF}{dD_c}. \tag{10}$$

Eq. (10) indicates that the friction stress can be measured from the slope of the measured pull-out force vs. punch displacement curve. It is noted that the negative signs in Eqs. (6), (9), and (10) reflect the fact that, according to our sign convention, the punch pull-out force F is negative and the frictional force, opposing the pull-out, is positive. In fact, the data segment dominated by frictional sliding between the punch sidewalls and molded hole conforms well to a linear fit, as indicated by the red lines shown in Fig. 5(b) and Fig. 6(b). Take the tool steel punch case as an example, the negative of the fitted slope in Fig. 5(b) is 1.07×10^{-4} mN/nm. Given R = 4.635 μm, this dataset thus yields a τ_f value of 3.7 MPa. Recognizing that σ_n may be a function of D, the τ_f value extracted from a linear fit to this data segment should be viewed as a value averaged over the entire punch/hole contact distance.

Fig. 9(a) shows values of the frictional slope, (-1)dF/dD, as a function of the maximum compression pressure P_{max}, together with its conversion into an average friction stress τ_f, for both the tool steel punch and the Ti64 punch data series. τ_f is seen to increase with increasing P_{max} in both cases. At P_{max} < 540 MPa, τ_f values for the Ti64 punch are either close to those for the tool steel punch or slightly higher, by ~ 30%. At P_{max} > 570 MPa, τ_f values for the Ti64 punch exhibit larger scatter, but exceed those for the tool steel punch significantly, 8 ~ 14 MPa for the former vs. < 6 MPa for the latter. The higher average friction stress for the Ti64 punch is again consistent with the expectation that Ti64 having a stronger interaction with Al as compared to tool steel.

According to Eq. (8), to obtain an average friction coefficient f from the τ_f data shown in Fig. 9(a) requires that the average normal stress or contact pressure σ_n be known. At this moment we are not aware of an elasto-plastic solution to this problem. In its absence, we turn to the classic problem of quasi-static expansion of spherical and cylindrical cavities in an infinite medium to obtain an estimate of the punch contact pressure [37]. The cavitation pressures for expansion of a small spherical cavity (P_s) or cylindrical cavity (P_c) in an infinite medium of elastic-perfectly plastic solid are given by Hill [37] as, respectively,

$$P_s = \frac{2Y}{3}\left\{1 + ln\left(\frac{E}{3(1-\upsilon)Y}\right)\right\}, \tag{11}$$

$$P_c = \frac{Y}{\sqrt{3}}\left\{1 + ln\left(\frac{\sqrt{3}E}{(5-4\upsilon)Y}\right)\right\}, \tag{12}$$

where E, ν, and Y are respectively Young's modulus, Poisson's ratio, and yield stress. Taking reasonable materials parameters corresponding to Al, E = 70 GPa, ν = 1/3, and Y = 100 MPa, we have $P_s \approx 4.57Y$ = 457 MPa, $P_c \approx 3.93Y$ = 393 MPa, and $(P_s - P_c)/P_c$ ~ 16%. Values of P_s and P_c calculated from Eqs. (11) and (12) are in reasonable correspondence with the lower end of the presently measured P_{max} values, ~470 MPa, corresponding to a D_{max} value of ~ 2000 nm. The increase in P_{max} at higher D_{max} values, 470 – 610 MPa, can be understood as a manifestation of strain hardening, which is absent from derivations of Eqs. (11) and (12) assuming elastic-perfectly plastic response. More recent solutions of the quasi-static cavity expansion problem yielded cavitation pressures largely in agreement with Hill's solution. For example, the solution of the cylindrical cavity expansion problem by Masri and Durban [38] gave

$$p_c = \frac{Y}{\sqrt{3}}\left\{1 + ln\left(\frac{\sqrt{3}E}{(4-2\upsilon)Y}\right)\right\}, \tag{13}$$

instead of Eq. (12). The difference in p_c values calculated from Eqs. (12) and (13) in the present case is ~ 1%. As pointed out by Hill, the cavitation pressure provides an estimate of the maximum resistive pressure in deep punch penetration into a quasi-infinite medium, which does not differ greatly with differing punch shape [37]. The reasonable correspondence between calculated cavitation pressure and measured values of P_{max} offers a justification for taking the latter as an estimate of the contact pressure between the punch and the molded Al near the end portion of the punch, while the punch is under the maximum compression load.

Fig. 9(b) plots the ratio τ_f/P_{max} vs. P_{max}. For the tool steel punch data series, values of τ_f/P_{max} stay relatively constant at ~ 0.65% within the P_{max} range of 470–580 MPa and increased slightly to ~ 0.8% at P_{max} of ~ 610 MPa. For the Ti64 punch data series, values of τ_f/P_{max} stayed above ~ 0.75% within the P_{max} range of 490–560 MPa and increased to > 1.5% at P_{max} > 580 MPa. The higher τ_f/P_{max} value for the Ti64 punch as compared to the tool steel punch again highlights the stronger interaction Ti64 has with Al. It is worth noting that the average contact pressure after complete unloading of the compression load, but with the punch still embedded within the Al specimen at the maximum molding depth, is expected to be different from that when the punch is still under

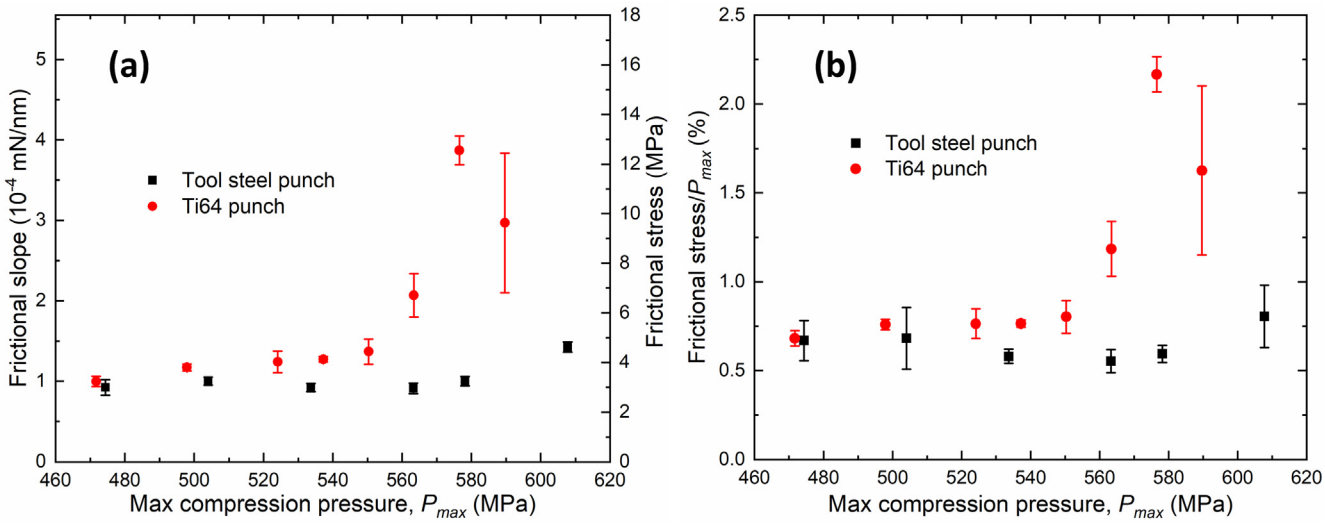

Fig. 9. Friction characteristics deduced from Al molding/demolding datasets: (a) the frictional slope and the average friction stress vs. P_{max} for the tool steel punch and the Ti64 punch; (b) the ratio between the average friction stress and P_{max} vs. P_{max}.

the maximum compression load. Specifically, the average sidewall contact pressure between the cylindrical punch and the molded specimen after complete unloading is expected to be smaller than the average contact pressure under the maximum compression load. Therefore, the effect of the compression unloading process on the sidewall contact pressure is considered next.

4.3. Friction coefficient estimation through finite element method (FEM) simulations

In the preceding section, we argued that the measured value of P_{max} can be taken as an estimate of the punch/specimen contact pressure when the punch is under the compression load L_{max}. To the best of our knowledge, neither an analytical solution nor a FEM solution exists for the sidewall contact pressure when a cylindrical punch is pushed into an elasto-plastic solid and then completely unloaded. To estimate the effect of compression unloading on the sidewall contact pressure, we assume that the compression unloading process is completely elastic. Accordingly, elastic FEM simulations were performed using the commercial code Abaqus® [39].

A cylindrical object with geometry conforming to the tool steel punch or the Ti64 punch was embedded into a large block approximating a semi-infinite medium, with the top surface of the cylinder flush with the medium top surface. The cylinder and the medium, approximating respectively the punch and the Al specimen, were assumed to be elastically isotropic. Axisymmetry was assumed. The boundaries between the cylinder and the medium were assumed to be perfectly bonded. Values of Young's modulus, E, and the Poisson's ratio, ν, for the tool steel punch, the Ti64 punch, and the aluminum matrix are given in Table 1. Due to rotational symmetry in the system geometry as well as loading and boundary conditions, the FEM simulations were conducted in a two-dimensional axisymmetric framework. The XYZ Cartesian coordinate system was transformed to a cylindrical coordinate system of $r\theta z$, and stress components were extracted from the FEM solutions.

Table 1
Isotropic elastic properties used in elastic FEM simulations.

Part	Young's modulus E (GPa)	Poisson's ratio ν
Cylinder 1 (tool steel)	210	0.3
Cylinder 2 (Ti64)	113	0.37
Medium (Al)	70	0.33

The process of punch elastic unloading is viewed as a cylinder, embedded within and flush with the top surface of the semi-infinite medium, subjected to two loads on the cylinder top surface: one of a compression pressure P_{max} and the other of a tensile traction of the same magnitude. The cylinder sidewall contact pressure or the radial stress component σ_{rr} at the cylinder sidewall surface is the quantity of interest. We again approximate the average sidewall contact pressure $< \sigma_{rr} >$ resulting from the compression load by P_{max}, in accordance with the cavity expansion model. The $< \sigma_{rr} >$ value due to the tensile traction of the cylinder top surface is calculated from the elastic FEM simulation. According to the principle of superposition, the average cylinder sidewall contact pressure at zero surface load should be an algebraic sum of P_{max} and the elastic $< \sigma_{rr} >$ value due to the tensile traction on the cylinder top surface.

As shown in Fig. 10(a), the system was constrained at the bottom along the Y direction in the Cartesian coordinate system or the Z direction in the cylindrical coordinate system. Also, the external load was applied as a traction distributed uniformly over a circular region on the top left of the aluminum half-space where the punch surface was located. In addition, the axis of symmetry was located on the left boundary, as shown in Fig. 10(a). The entire simulation system was a square with 500 units of length in both X and Y directions, and the cylinders had 10 units of length in radius with depths adjusted to the values used in the experiments, such that the ratio of the cylinder depths over their diameters were kept the same as those in the experiments. To capture the stress concentrations and gradients more accurately around the cylindrical punch/half-space boundaries and the regions under the load, the structured mesh generation was biased toward these regions such that a finer mesh was obtained around the punch, as illustrated in Fig. 10(b) and (c). Eight-node biquadratic axisymmetric quadrilateral elements were employed in the finite element mesh, as quadratic elements are suitable for problems with discontinuity in the primary field (or the gradients of the primary field) and problems in which it is highly likely to have regions with stress concertation [40]. Considering different depth over radius ratios for the cylindrical punches used in the experiments and doing convergence analysis to find the sufficient number of elements, 99,231 to 157,552

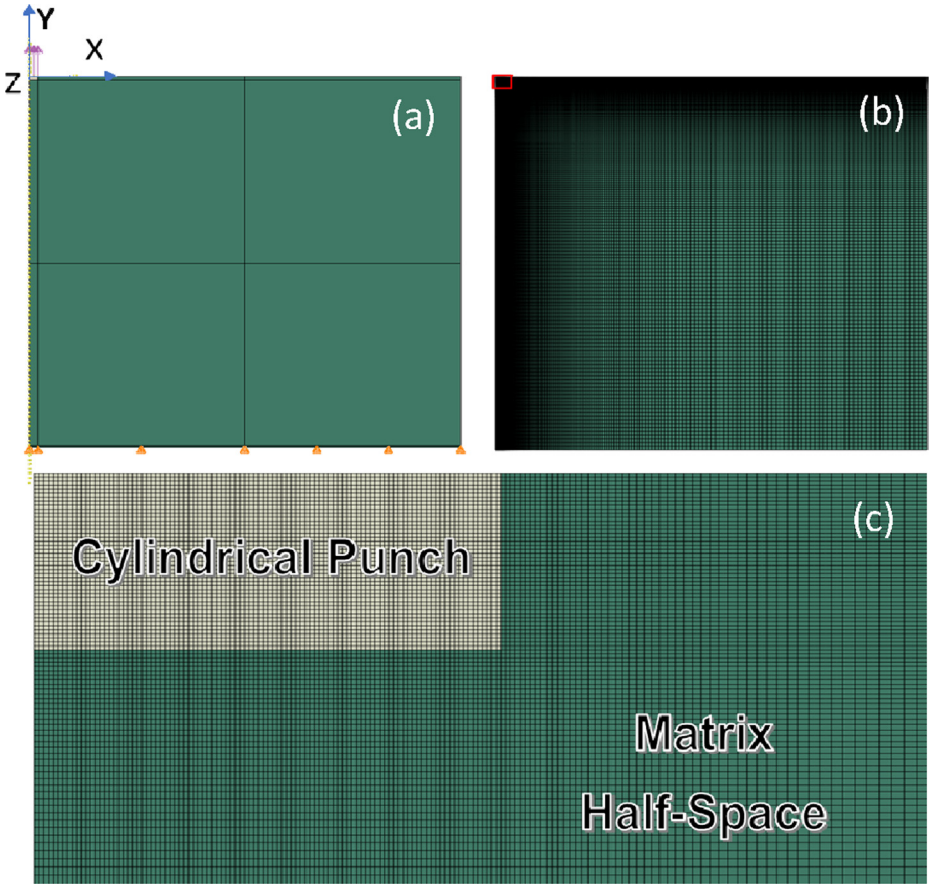

Fig. 10. Setup and boundary conditions related to elastic FEM simulations of cylindrical tool steel and Ti64 punches embedded in an aluminum half-space: (a) geometry, loading condition, and boundary condition; (b) a finite element mesh used for the axisymmetric bi-material system; (c) a magnified image of the area indicated by the red rectangular frame shown in (b). (For interpretation of the references to colour in this figure legend, the reader is referred to the web version of this article.)

number of elements were utilized to obtain FEM solutions for the punches with different sizes, e.g., for the cylindrical punch with the largest embedded depth, 157,552 elements were used.

While the matrix half-space extends to infinity in theory, in practice however, a finite sized punch/half-space simulation system has to be chosen. To ensure that the finite size of the simulation does not disturb significantly the stress field in the region of interest, i.e., the region around the punch/half-space boundary, the setup shown in Fig. 10 was used to compare the FEM solution (with the minimum number of 99,231 elements) to the Boussinesq solution for the distribution of stresses in a half-space resulting from a uniform surface compression load [41], when the direction of the load shown in Fig. 10(a) was reversed and the elastic properties of the cylindrical punch region were set to be identical to those of the matrix. The result of the FEM solution is depicted in Fig. 11(a) against the Boussinesq solution for the vertical stress, σ_{zz}, in the cylindrical coordinate system on the axis of symmetry. The results were presented for the vertical stress normalized by the applied uniform pressure versus the depth H measured from the top surface of the half-space normalized by the radius of the circularly loaded area R. As evident from Fig. 11(a) and (b) and regarding the Saint-Venant's principle, the FEM solution is in excellent agreement with the analytical Boussinesq solution up to an H/R ratio of 20, which is far away from the regions of interest with respect to the cylindrical punches' radii and depths. Therefore, the stress field in the regions of interest should not be affected due to the limited size of the simulation. It should also be noted that the errors that are increasing after an H/R ratio of 20 in Fig. 11(b) are related to the very small stress magnitudes shown in Fig. 11(a), and they will not affect the solution in the region of interest around the cylindrical punch/half-space boundary. In addition, in Fig. 11(c), contours of vertical stress or bulbs of pressure for vertical stress beneath the uniformly loaded circular area have been provided, and it can be observed that the FEM solution reproduces well the Boussinesq bulbs of pressure [41].

For each FEM simulation, a uniform tensile traction corresponding to the P_{max} value needed to achieve D_{max} was applied to the top surface of the cylinder, resulting in a pull of the cylinder out of the medium. To extract the average sidewall radial stress, or $< \sigma_{rr} >$, values from the FEM result, only the bottom 20% of the depth of the embedded punch was considered. Specifically, the column of elements associated with the cylindrical punch located at the punch/half-space boundary were considered. The $< \sigma_{rr} >$ values were obtained from averaging σ_{rr} at integration points over the elements contributing to the bottom 20% of the punch depth. Detailed simulation geometries and resulting outputs are listed in Table 2. We take the value of $|P_{max} + <\sigma_{rr}>|$ as an estimate of the punch/matrix sidewall contact pressure after complete compression unloading, i.e., $\sigma_n \approx |P_{max} + <\sigma_{rr}>|$. It is noted that averaging only the bottom 20% of the cylinder height to obtain $< \sigma_{rr} >$ is in accordance with the experimental observations shown in Fig. 7(c). The value of τ_f/σ_n was taken as an estimate of the average friction coefficient, f. A plot of f vs. P_{max} is shown in Fig. 12. The values of f are only slightly increased as compared to values of τ_f/P_{max}: staying at ~ 0.01 for the steel punch case and reaching ~ 0.02 for the Ti64 punch case at P_{max} over 550 MPa.

To the best of our knowledge, the present results represent the first direct friction force measurement and friction coefficient esti-

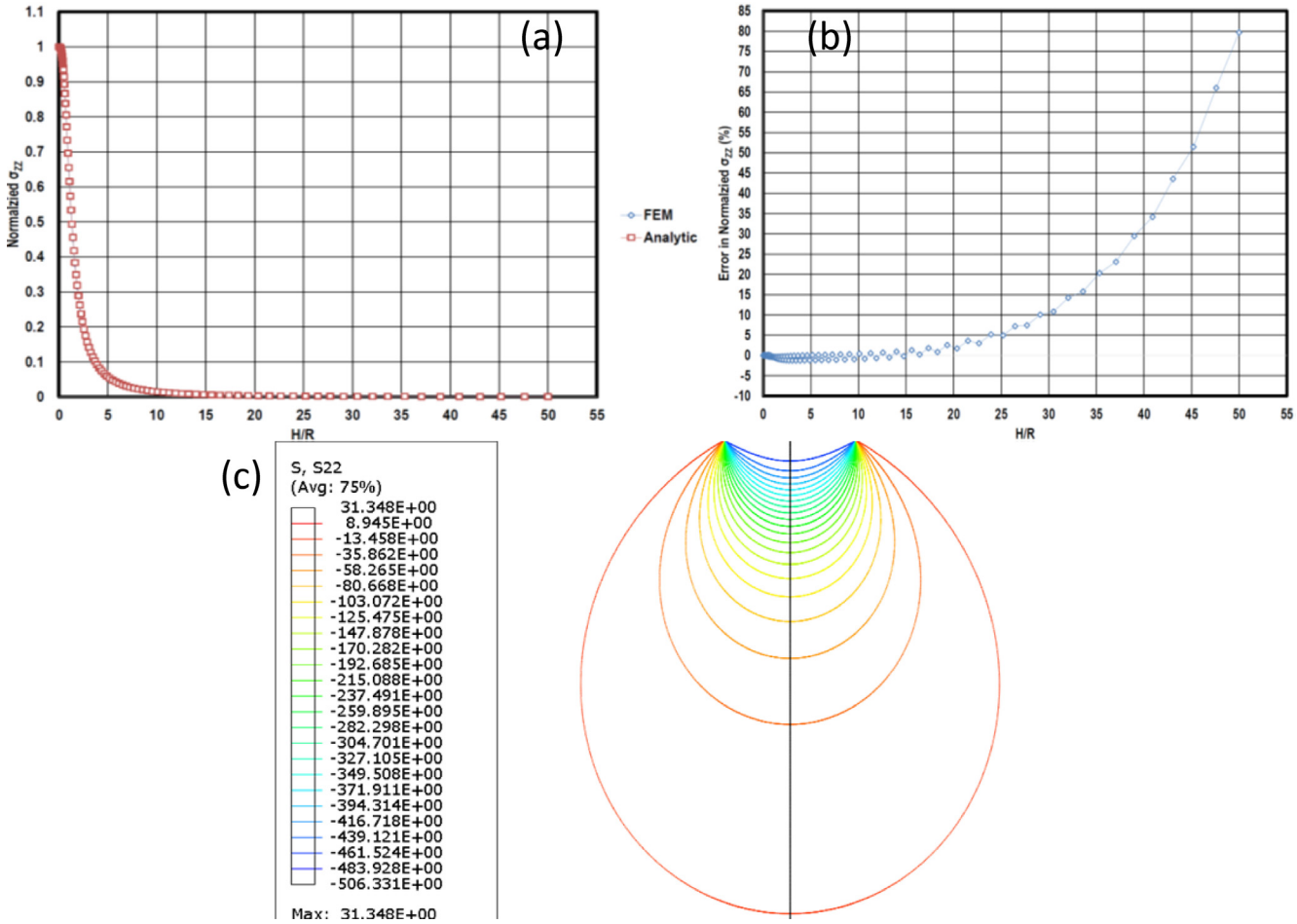

Fig. 11. (a) Comparison between the FEM solution and the analytical Boussinesq solution for vertical stress or σ_{zz} profile on the axis of symmetry; (b) errors in the FEM solution as compared to the analytical Boussinesq solution for vertical stress or σ_{zz} profile on the axis of symmetry; (c) contour of vertical stress or bulbs of pressure for vertical stress beneath the uniformly loaded circular area.

Table 2
Elastic FEM simulation geometries and result outputs

Cylinder 1 (tool steel punch)		
Applied surface tensile traction P_{max} (MPa)	Embedded punch depth over punch diameter D_{max} (μm)/(2R) (μm)	Radial stress averaged over the bottom 20% of punch depth $\langle\sigma_{rr}\rangle$ (MPa)
474.37	0.221	122.61
504.02	0.291	97.67
533.67	0.381	70.68
563.32	0.510	42.53
578.14	0.648	43.65
607.79	0.943	4.45
Cylinder 2 (Ti64 punch)		
471.71	0.251	119.24
497.92	0.346	95.08
524.13	0.470	68.56
537.23	0.532	58.20
550.33	0.697	36.19
563.44	0.829	24.84
576.54	1.008	14.91
589.64	1.099	11.66

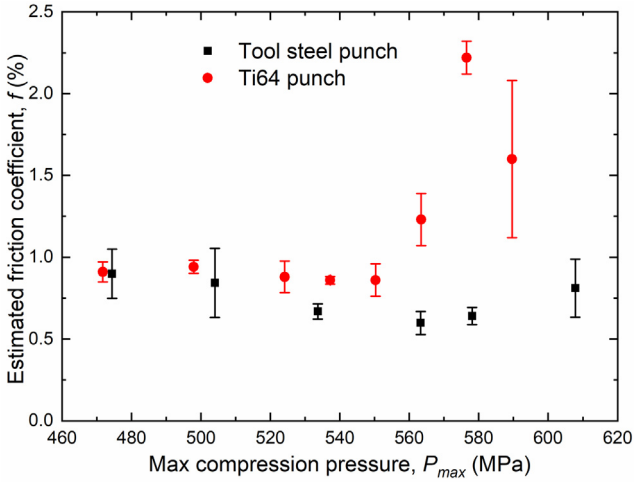

Fig. 12. The estimated average friction coefficient f vs. P_{max}.

mate under dry contact conditions in micron scale metal forming operations. The estimated average friction coefficient is 0.01–0.02, comparable with values from macroscale friction tests with lubricants. For instance, friction coefficient, measured by Groche et al. using six established macroscale tribological tests with lubricants, varied within a range of 0.02 to 0.07 [16]. Generally, friction coefficients under dry conditions tend to be higher than that with lubricants. One data point was given by Wang et al., who found a friction coefficient of 0.15 in dry metal forming using Al specimen and a DLC coated tool [24]. Given that the punches used in the present CMDT experiments possessed rather smooth surfaces, the low value of friction coefficient obtained here may be ascribed in part

to a much reduced surface roughness resulting from the FIB milling fabrication process [27]. The presence of a slight taper in the cylindrical punches as evidenced by data shown in Fig. 7(c), albeit an indirect one, may further contribute to the low apparent friction coefficient.

4.4. CMDT method assessment

Limitations of the present set of load-controlled measurements should be noted. As shown in Fig. 3(c), that $|\dot{L}|$ values after t = 162.1119 s do not remain identically zero, while the actuator was executing rapid oscillations of significant amplitudes, gives an indication of the efficacy and limitations of the actuator dynamics model when it is moving at significantly higher speeds and accelerations as compared to typical indentation experiments, e.g., speed < 0.4 nm/ms as shown in Fig. 4(b). Such limitations notwithstanding, we believe that the present datasets, measured for both the tool steel punch and the Ti64 punch, are physically sound and do provide sufficient details to elucidate the actual punch disengagement processes. In the future, the load-controlled loading/unloading mode used in the present work can potentially be switched to a displacement-controlled mode for more stable and accurate measurements.

The present work demonstrates that CMDT offers a new method to measure stiction and friction in microscale metal forming operations with a number of advantages. The first advantage lies in its simplicity of operation. CMDT involves merely a microscale cylindrical punch and can be easily performed in situ an SEM. Its high precision in force measurements constitutes the second advantage, especially over scaled-down versions of macroscale friction measurements mentioned in the introduction. The third advantage lies in its wide applicability. For instance, the diameter of cylindrical punches is adjustable over a wide range, from tens of microns to submicron, offering the potential of generating new and direct experimental evidence of specimen size effect on microscale friction, either with lubricants or under dry contact conditions.

It is also worth noting that the present CMDT approach stands to be improved in at least two aspects. First, the presence of a slight taper in the cylindrical punches resulting from the FIB milling procedure limits the extent of punch/specimen sidewall contact. It is therefore highly desirable to develop an alternative punch fabrication protocol that would result in a geometrically more ideal cylindrical punch. Second, the model of cavity expansion in an infinite medium was used in the absence of an elasto-plastic solution, which increases the uncertainties in the friction coefficient estimation. Thus, the development of new models to better address the contact conditions between the cylindrical punch and the molded specimen would be most helpful [42]. Both aspects await future investigation.

5. Conclusions

In this work, we present an alternative method, CMDT, to measure and analyze stiction and friction in microscale metal forming operations. The main conclusions are summarized as follows:

(1) Instrumented microscale molding and demolding of a single crystal Al specimen with cylindrical tool steel and Ti64 punches were conducted in-situ an SEM. Stiction and friction forces during punch/specimen disengagement were measured. The present measurements, to the best of our knowledge, represent the first direct measurement of stiction and friction forces under dry contact conditions for microscale metal forming operations.

(2) Average stiction and friction stresses were deduced from raw stiction and friction forces and were observed for both tool steel punch and Ti64 punch to increase as the maximum compression pressure increased. Stiction stress values (2–8 MPa) are consistent with previous results from CBA and AFM measurements. Friction stress measured for the Ti64 punch is higher than that for the tool steel punch.

(3) Sidewall contact pressure between the cylindrical punch and the molded aluminum was estimated by combining the cavity expansion model and elastic FEM simulations. The estimated average friction coefficient is 0.01–0.02, a relatively low value due potentially to a combination of the rather smooth punch surfaces with the presence of a slight taper on the punch. Ti64 punch presents a higher average friction coefficient as compared to that for the tool steel punch.

(4) CMDT possesses advantages such as high operation simplicity, high measurement precision, and wide applicability, and offers an alternative approach for quantitative assessment of friction in a variety of microscale metal forming problems.

Data availability

The raw/processed data required to reproduce the present findings cannot be shared at this time as the data also forms a part of another ongoing study. Raw and processed data can be made available at a later time from the first author and the corresponding author upon reasonable request.

CRediT authorship contribution statement

Bin Zhang: Methodology, Investigation, Data curation, Formal analysis, Writing – original draft, Writing – review & editing. **Reza Namakian:** Data curation, Formal analysis, Writing – original draft. **Xiaoman Zhang:** Methodology, Investigation, Data curation. **W.J. Meng:** Conceptualization, Methodology, Investigation, Data curation, Formal analysis, Writing – original draft, Writing – review & editing, Supervision, Funding acquisition. **Jennifer Hay:** Data curation, Formal analysis, Writing – original draft. **Kurt Johanns:** Data curation, Formal analysis, Writing – original draft.

Declaration of Competing Interest

The authors declare that they have no known competing financial interests or personal relationships that could have appeared to influence the work reported in this paper.

Acknowledgments

The authors gratefully acknowledge partial project support from the U.S. National Science Foundation under awards NSF OIA-1541079 and OIA-1946231. Utilization of experimental facilities housed within the LSU Shared Instrumentation Facilities (SIF), a part of the NSF EPSCoR core user facilities (CUF), is acknowledged. WJM acknowledges helpful discussions with Prof. J.W. Hutchinson with thanks.

References

[1] M.P. Groover, Fundamentals of modern manufacturing: materials, processes, and systems, John Wiley & Sons, 2020.
[2] E.-S. Yoon, R.A. Singh, H.-J. Oh, H. Kong, The effect of contact area on nano/micro-scale friction, Wear. 259 (2005) 1424–1431, https://doi.org/10.1016/j.wear.2005.01.033.
[3] W. Zheng, G. Wang, G. Zhao, D. Wei, Z. Jiang, Modeling and analysis of dry friction in micro-forming of metals, Tribol. Int. 57 (2013) 202–209.

[4] L. Wang, H. Yang, Friction in aluminium extrusion—part 2: A review of friction models for aluminium extrusion, Tribol. Int. 56 (2012) 99–106.
[5] C.V. Nielsen, N. Bay, Review of friction modeling in metal forming processes, J. Mater. Process. Technol. 255 (2018) 234–241, https://doi.org/10.1016/j.jmatprotec.2017.12.023.
[6] J.T. Black, R.A. Kohser, DeGarmo's materials and processes in manufacturing, John Wiley & Sons, 2020.
[7] C. Hu, Q. Yin, Z. Zhao, H. Ou, A new measuring method for friction factor by using ring with inner boss compression test, Int. J. Mech. Sci. 123 (2017) 133–140.
[8] Z.G. Wang, S. Komiyama, Y. Yoshikawa, T. Suzuki, K. Osakada, Evaluation of lubricants without zinc phosphate precoat in multi-stage cold forging, CIRP Ann. 64 (1) (2015) 285–288.
[9] C. Hu, H. Ou, Z. Zhao, An alternative evaluation method for friction condition in cold forging by ring with boss compression test, J. Mater. Process. Technol. 224 (2015) 18–25.
[10] P. Groche, J. Stahlmann, C. Müller, Mechanical conditions in bulk metal forming tribometers—Part two, Tribol. Int. 66 (2013) 345–351.
[11] S.-H. Kang, K. Seok Lee, Y.-S. Lee, Evaluation of interfacial friction condition by boss and rib test based on backward extrusion, Int. J. Mech. Sci. 53 (2011) 59–64, https://doi.org/10.1016/j.ijmecsci.2010.11.001.
[12] Y. Zhu, W. Zeng, X. Ma, Q. Tai, Z. Li, X. Li, Determination of the friction factor of Ti-6Al-4V titanium alloy in hot forging by means of ring-compression test using FEM, Tribol. Int. 44 (12) (2011) 2074–2080.
[13] A. Buschhausen, K. Weinmann, J.Y. Lee, T. Altan, Evaluation of lubrication and friction in cold forging using a double backward-extrusion process, J. Mater. Process. Technol. 33 (1-2) (1992) 95–108.
[14] C. Hu, Q. Yin, Z. Zhao, A novel method for determining friction in cold forging of complex parts using a steady combined forward and backward extrusion test, J. Mater. Process. Technol. 249 (2017) 57–66, https://doi.org/10.1016/j.jmatprotec.2017.06.001.
[15] L. Lazzarotto, L. Dubar, A. Dubois, P. Ravassard, J. Oudin, Identification of Coulomb's friction coefficient in real contact conditions applied to a wire drawing process, Wear. 211 (1) (1997) 54–63.
[16] P. Groche, P. Kramer, N. Bay, P. Christiansen, L. Dubar, K. Hayakawa, C. Hu, K. Kitamura, P. Moreau, Friction coefficients in cold forging: A global perspective, CIRP Ann. 67 (2018) 261–264, https://doi.org/10.1016/j.cirp.2018.04.106.
[17] B. Zhang, W.J. Meng, Effects of punch geometry and grain size in micron scale compression molding of copper, Mater. Des. 206 (2021), https://doi.org/10.1016/j.matdes.2021.109807.
[18] B. Zhang, M. Dodaran, S. Ahmed, S. Shao, W.J. Meng, K.J. Juul, K.L. Nielsen, Grain-size affected mechanical response and deformation behavior in microscale reverse extrusion, Materialia 6 (2019), https://doi.org/10.1016/j.mtla.2019.100272.
[19] B. Zhang, Y. Song, G.Z. Voyiadjis, W.J. Meng, Assessing texture development and mechanical response in microscale reverse extrusion of copper, J. Mater. Res. 33 (8) (2018) 978–988.
[20] M.W. Fu, J.L. Wang, Size effects in multi-scale materials processing and manufacturing, Int. J. Mach. Tools Manuf. 167 (2021) 103755, https://doi.org/10.1016/j.ijmachtools.2021.103755.
[21] U. Engel, R. Eckstein, Microforming—from basic research to its realization, J. Mater. Process. Technol. 125–126 (2002) 35–44, https://doi.org/10.1016/S0924-0136(02)00415-6.
[22] U. Engel, Tribology in microforming, Wear 260 (2006) 265–273, https://doi.org/10.1016/j.wear.2005.04.021.
[23] N. Tiesler, Grundlegende Untersuchungen zum Fließpressen metallischer Kleinstteile, Meisenbach, 2002. https://opus4.kobv.de/opus4-fau/frontdoor/index/index/docId/13073.
[24] Z.G. Wang, Y. Yoshikawa, T. Suzuki, K. Osakada, Determination of friction law in dry metal forming with DLC coated tool, CIRP Ann. 63 (1) (2014) 277–280.
[25] Z. Wang, T. Suzuki, Friction law in dry metal forming of materials with work hardening, Procedia Manuf. 15 (2018) 475–480, https://doi.org/10.1016/j.promfg.2018.07.253.
[26] F. Flegler, S. Neuhäuser, P. Groche, Influence of sheet metal texture on the adhesive wear and friction behaviour of EN AW-5083 aluminum under dry and starved lubrication, Tribol. Int. 141 (2020) 105956, https://doi.org/10.1016/j.triboint.2019.105956.
[27] M.D. Uchic, P.A. Shade, D.M. Dimiduk, Plasticity of micrometer-scale single crystals in compression, Annu. Rev. Mater. Res. 39 (1) (2009) 361–386.
[28] B. Zhang, M.S. Dodaran, S. Shao, J. Choi, S. Park, W.J. Meng, Understanding of plasticity size-effect governed mechanical response and incomplete die filling in a microscale double-punch molding configuration, Int. J. Mech. Sci. 172 (2020) 105406, https://doi.org/10.1016/j.ijmecsci.2019.105406.
[29] I. Hutchings, P. Shipway, Tribology: friction and wear of engineering materials, Butterworth-Heinemann, 2017.
[30] M.J. Madou, Fundamentals of microfabrication: the science of miniaturization, CRC press, 2018.
[31] N. Tas, T. Sonnenberg, H. Jansen, R. Legtenberg, M. Elwenspoek, Stiction in surface micromachining, J. Micromech. Microeng.. 6 (4) (1996) 385–397.
[32] M.R. Houston, R.T. Howe, R. Maboudian, Effect of hydrogen termination on the work of adhesion between rough polycrystalline silicon surfaces, J. Appl. Phys. 81 (8) (1997) 3474–3483.
[33] U. Srinivasan, M.R. Houston, R.T. Howe, R. Maboudian, Alkyltrichlorosilane-based self-assembled monolayer films for stiction reduction in silicon micromachines, J. Microelectromech. Syst. 7 (2) (1998) 252–260.
[34] I. Szlufarska, M. Chandross, R.W. Carpick, Recent advances in single-asperity nanotribology, J. Phys. D. Appl. Phys. 41 (12) (2008) 123001, https://doi.org/10.1088/0022-3727/41/12/123001.
[35] Y. Jiang, K.T. Turner, Measurement of the strength and range of adhesion using atomic force microscopy, Extrem. Mech. Lett. 9 (2016) 119–126.
[36] O. Kubaschewski, G. Heymer, Heats of formation of transition-metal aluminides, Trans. Faraday Soc. 56 (1960) 473–478.
[37] R. Hill, The mathematical theory of plasticity, Oxford university press, 1998.
[38] R. Masri, D. Durban, Quasi-static cylindrical cavity expansion in an elastoplastic compressible Mises solid, Int. J. Solids Struct. 43 (25-26) (2006) 7518–7533.
[39] Abaqus, Dassault Systems, (2020). http://www.3ds.com/products-%09services/simulia/products/abaqus/.
[40] R. Namakian, H.M. Shodja, M. Mashayekhi, Fully enriched weight functions in mesh-free methods for the analysis of linear elastic fracture mechanics problems, Eng. Anal. Bound. Elem. 43 (2014) 1–18.
[41] I. Smith, Smith's elements of soil mechanics, John Wiley & Sons, 2014.
[42] T. Shimizu, M. Yang, K. Manabe, Classification of mesoscopic tribological properties under dry sliding friction for microforming operation, Wear 330–331 (2015) 49–58, https://doi.org/10.1016/j.wear.2015.01.050.